Velocity-space sensitivity and inversions of synthetic ion cyclotron emission

B. S. Schmidt,[1] M. Salewski,[1] B. C. G. Reman,[1, a)] R. O. Dendy,[2] Y. Dong,[3] H. Järleblad,[1] D. Moseev,[4] R. Ochoukov,[5] M. Rud,[1] and A. Valentini[1]

[1)]*Department of Physics, Technical University of Denmark, Kgs. Lyngby, 2800, Denmark*
[2)]*Centre for Fusion, Space and Astrophysics, University of Warwick, Coventry, CV4 7AL, United Kingdom*
[3)]*Department of Applied Mathematics and Computer Science, Technical University of Denmark, Kgs. Lyngby, 2800, Denmark*
[4)]*IPP Greifswald, Max-Planck-Institut für Plasmaphysik, Greifswald, 17491, Germany*
[5)]*IPP Garching, Max-Planck-Institute für Plasmaphysik, Garching, 85748, Germany*

(*Electronic mail: bossc@dtu.dk, msal@dtu.dk, bcgre@fysik.dtu.dk, R.Dendy@warwick.ac.uk, yido@dtu.dk, henrikj@dtu.dk) (Dmitry.moseev@ipp.mpg.de, roman.ochoukov@ipp.mpg.de, mrula@dtu.dk, anvalen@fysik.dtu.dk)

(Dated: 5 August 2023)

This paper introduces a new model to find the velocity-space location of energetic ions generating ion cyclotron emission (ICE) in plasmas. ICE is thought to be generated due to inverted gradients in the $v_\perp$ direction of the velocity distribution function or due to anisotropies, i.e., strong gradients in the pitch direction. Here, we invert synthetic ICE spectra generated from first principles PIC-hybrid computations to find the locations of these ICE-generating ions in velocity space in terms of a probability distribution function. To this end, we compute 2D ICE weight functions based on the magnetoacoustic cyclotron instability which reveals the velocity-space sensitivity of ICE measurements. As an example, we analyze the velocity-space sensitivity of synthetic ICE measurements near the first 15 harmonics for plasma parameters typical for the Large Helical Device. Further, we investigate the applicability of a least-square subset search, Tikhonov regularization, and Lasso regularization to obtain the locations in velocity space of the ions generating the ICE.

I. INTRODUCTION

Ion cyclotron emission (ICE) refers to strongly superthermal radiation in the ion cyclotron range of frequencies (ICRF), typically with well-defined power spectral peaks associated with harmonics of the local cyclotron frequency of a minority energetic ion population within the plasma. ICE has been detected using externally mounted antennas and probes, and also recently by internal scattering[1]. It can exhibit both predominantly electromagnetic or electrostatic characteristics[2,3]; in both cases, it appears to be driven by collective relaxation of the energetic ions under the magnetoacoustic cyclotron instability (MCI). In tokamaks, MCIs can, for example, be driven by marginally-trapped fusion products born in the center of the plasma with a radial drift to the outer edge of the plasma[4]. The velocity distribution of the fusion products from the location emitting the ICE contains anisotropies or inverted gradients in the form of a local maximum in pitch or energy. Such anisotropies and inverted gradients contain free energy to drive the MCI.

An ICE diagnostic is a passive non-invasive diagnostic. It is possible to measure characteristics of fast ions and of phenomena producing signals in the ion-cyclotron frequency range such as compressional Alfvén eigenmodes (CAEs) and global Alfvén eigenmodes (GAEs) with ICE detectors[5–12]. The diagnostic is compatible with high-radiation environments such as in ITER, e.g., by using the antennas for electromagnetic wave heating in the ion cyclotron range of frequencies (ICRF) as receivers[3,13].

ICE refers to the signal generated at integer multiples of the ion cyclotron frequency of the ion species generating it. Including the Doppler shift, the resonance condition of the ICE-generating ions is

$$\omega = n\Omega_s + v_\parallel k_\parallel, \tag{1}$$

where n is a positive integer, Ω_s is the cyclotron frequency for the ion species s, $v_\parallel$ is the velocity of the ions parallel to the magnetic field, and $k_\parallel$ is the parallel wave number. Typically, the frequency of the fundamental harmonic is around 10 MHz depending on the magnetic field and species[14].

Studies at JET in the early 1990s discovered a linear relationship between the ICE signal intensity and the neutron emission rate from DT reactions by comparing ICE from DD and DT plasmas heated using neutral beam injection (NBI)[5]. They concluded that fusion α-particles were responsible for providing the free energy to generate ICE localized at the outer midplane edge of the plasma, near the last closed flux surface. Measurements at LHD also detected ICE from lost ions at the plasma edge during perpendicular hydrogen NBI and from ions lost due to toroidicity-induced Alfvén eigenmode (TAE) bursts[6]. Recently, an ICE detector has been installed at Wendelstein 7-X[15]. Empirical studies of ICE have been performed at many different devices, including JET[5,16,17], TFTR[18], KSTAR[19–21], ASDEX-U[14,22], LHD[23–28], JT-60U[29–31], DIII-D[32–34], and EAST[35]. Further, beam-heated plasmas on several tokamaks emit core ICE signals generated by the MCI driven by the velocity-space inversion of sub-Alfvénic beam-injected ions[14,36]. Thus, ICE signals provide

[a)] Also at Centre for Fusion, Space and Astrophysics, University of Warwick, Coventry, CV4 7AL, United Kingdom

helpful information for diagnosing fast-ion behavior.

We want to infer the location of the source of the ICE in velocity space from measured ICE signals. Research over the last decade has inferred 2D fast-ion velocity distribution functions for diagnostics such as FIDA spectroscopy[37–44], collective Thomson scattering (CTS)[45], neutron emission spectrometry (NES)[46,47], γ-ray spectrometry (GRS)[46,47], and scintillator-based fast-ion loss detectors (FILDs)[48,49] at tokamaks such as ASDEX Upgrade, JET, EAST, DIII-D, and MAST. For these diagnostics, the 2D fast-ion velocity distribution function is determined from measurements by solving an inverse problem. The technique is called 'velocity-space tomography.' In addition to 2D velocity distribution functions, velocity-space tomography has inferred 1D velocity distribution functions of FIDA[50] measurements, synthetic ICE measurements[51], and 3D phase-space distributions of all energetic particle orbits based on FIDA measurements[52]. Such inversions require knowledge of the velocity-space sensitivity of the diagnostics, which is encoded in weight functions. Weight functions have been developed for most of the abovementioned diagnostics, including FIDA[53,54], neutral particle analyzers (NPA)[54], CTS[55], FILDs[56], GRS[57,58], NES[59–63], and 3 MeV proton diagnostics[64].

The conceptual framework, interpretation, and practical implementation of the 2D ICE weight function formalism to obtain the locations of the ions generating the ICE in velocity space from ICE signals are developed in this paper. In section 2, we describe our simulation code, and it is argued, based on results from ICE experiments and simulations, that ICE weight functions can be computed for ICE arising from a single ring-beam fast ion distribution function. In section 3, a new model for the inference of the location of the ICE source is presented. In section 4, the generation of the 2D weight functions is explained. In section 5, the velocity-space sensitivity quantified by ICE weight functions is interpreted. In section 6, the locations of the ions generating the ICE in velocity space are obtained by applying a subset search, Tikhonov regularization, and Lasso regularization to synthetic ICE signals. In section 7, a conclusion and future outlook are given.

II. MODELLING OF ICE

Our investigations are based on numerical solutions of the Maxwell-Lorentz system of equations. We track the velocity-space trajectories, including the gyromotion, of millions of kinetic energetic and thermal ions, alongside the three components of the evolving electric and magnetic fields, with a massless electron fluid using a nonlinear 1D3V PIC-hybrid particle-in-cell code. This coupling of the ions, fluid electrons, and fields is achieved through the Lorentz force and Maxwell's equations in Darwin's approximation[65]. Notably, the model is quasineutral and this approach bypasses the need to resolve the Debye length. This hybrid-PIC approach has previously been used successfully for the interpretation of ICE spectra from plasmas in the LHD heliotron-stellarator, addressing physics issues including super-Alfvénic versus sub-Alfvénic ion populations driving ICE[28], dependence of ICE spectra on local plasma density[66], and the role of trace fusion-born ions[67]; see also Refs.[27,68,69].

ICE is thought to be generated by inverted gradients in velocity space or anisotropies. Often a ring distribution is used to model ICE[70]. We use a ring distribution as a proxy for more complicated distributions functions such as those simulated with TRANSP, see, e.g., Ref.[36]. It is then investigated if this ring distribution drives ICE by solving a dispersion relation or Maxwell-Vlasov equations, and this rests on the identification of a subset of energetic ions. Additionally, the emission location or resonance condition needs to be identified. When several peaks are present, this is usually inferred from the spectral spacing taken to correspond to the fundamental cyclotron frequency of the emitting species under the assumption of drive by a single species at a given location. Disambiguation of ICE has been achieved in the presence of one single spectral peak; see, for example, refs.[14,31], and in the presence of multiple energetic ion species; see, for example, refs.[71–74]. Once a likely emission location with an inversion or a strong anisotropy has been identified, a particle-in-cell (PIC) simulation in the local approximation can be set up to study the fast collisionless relaxation of energetic ions under the MCI[75,76] from which the linear phase is compared with theory[2,77], synthetic spectra are calculated, and the non-linear phase investigated by higher order spectral methods[76,78]. It is important to note that, in experiment, a detector will have a finite acceptance cone for the propagation angles of the fast Alfvén waves, i.e., a range of **k**s, whereas our simulations assume just one angle is measured. Thus, our hybrid simulations do not have an exact one-to-one correspondence with experimental ICE measurements.

Also, a detector will likely have some wavenumber sensitivity depending on the emission location and on the detector geometry. The power spectra in the hybrid PIC simulations are calculated by integrating over the magnitude of k at one fixed wavevector direction. However, the intensity is highly localised in (w,k)-space through the MCI, when the resonance occurs predominantly on the fast Alfvén wave branch. Therefore, it is possible from the simulations to identify which regions in terms of the magnitude of k contribute the most to the power spectrum and where they are localised such as on the fast Alfvén branch[66,79]. The simulated power spectrum may be different from a measured one due to the frequency and wavenumber response function of the detector. We assume here the ideal case of identical wavenumber sensitivity for all wavenumbers.

Complementary to comparing measured ICE spectra to simulated ICE spectra, obtained in the nonlinear saturated regime from PIC-type computations, one may also compare the time evolution of measured ICE spectra to linear growth rates obtained from MCI theory. Such an approach was first applied[80] for TFTR (for sub-Alfvénic MCI with finite $k_\parallel$) and more recently in ASDEX Upgrade core ICE driven by sub-Alfvénic energetic deuterons in deuterium plasmas[14] and by sub-Alfvénic fast hydrogen in helium plasmas[36]. In these studies at ASDEX Upgrade, TRANSP simulations of NBI show three peaks at the full, half, and third of the injection energy. In the modelling, the growth rates were evaluated using cold ring distributions located at the full-energy beam

peak in velocity space. The propagation angle of the ICE was constrained by maximising growth rate and avoiding strong wave reabsorption in the plasma. Recent PIC simulations have shown that several energetic ion populations can simultaneously drive the MCI and also interact with it. This is true for beam-driven MCI and the beam ions interacting with the MCI[27] but also for beam ions driving the MCI interacting with an energetic thermal ion population (100 keV helium ash α-particles)[81]. Therefore, this questions the relaxation of single ring distributions for NBI studies. However, the beam deposition profile is energy dependent, so two fast ion populations may not reach their maximum density at the same radial position[82], thereby minimising such interactions. If one is interested in finding where in velocity space instability occurs, it will usually be dictated by the maximum energy component, provided an inverted gradient in velocity space exists in that region. Therefore, as indicated by simulations, ICE in the presence of beam interaction will still be strongly driven, possibly affecting the spectral properties, but not as much if the beam density profiles peak at different locations. This motivates the calculation of weight functions arising from a single ring distribution of fast ions in this work.

The physical parameters correspond to those of the LHD edge given in refs.[51,67]: the magnitude of the background magnetic field is $B_0 = 1.75$ T, electron density $n_e = 0.9\times10^{19}$ m^{-3}, and thermal electron and deuteron temperatures $T_e = 800$ eV and $T_D = 900$ eV. The hybrid PIC simulations[68,69,83] initialise the background thermal deuterons and ring distributed protons on a 1D grid consisting of 2048 cells using a quiet start for the thermal deuterons. Each ion species is represented by 500 macroparticles per cell. This approach assumes that the physics embodied in the PIC-hybrid simulations dominates the generation of the observed ICE signals, and this appears to be well grounded[75]. We note, however, that further experimental validation on the role of the spatial eigenfunction is still needed. These simulations are followed through the linear phase of the MCI and then deeply into its non-linear saturated phase. The energetic protons are initialized uniformly and randomly in space with velocities following a cold ring distribution $f_{\mathrm{CR}}(v_\parallel, v_\perp) = n_{\mathrm{H}}\delta\left(v_\parallel - u_\parallel\right)\delta\left(v_\perp - u_\perp\right)$ to generate the inversion with $u_\perp = [0.6 : 0.1 : 2.6]\ v_{\mathrm{A}}$ and $u_\parallel = [-2.6 : 0.1 : 2.6]\ v_{\mathrm{A}}$, where $v_{\mathrm{A}} = 0.9\times10^7$ m s^{-1} is the Alfvén speed at the emission location. Carrying out a full scan over $(u_\parallel, u_\perp)$ equates to scanning over $(v_\parallel, v_\perp)$ and for convenience we use the latter variables from here on. The calculations are carried over 60 proton gyroperiods, ensuring saturation of the MCI across every simulation for a relative energetic proton density $n_{\mathrm{H}}/n_{\mathrm{e}} = 1.75\times10^{-3}$. The relaxation of the energetic protons through the MCI generates excitations of the magnetic fields at multiple cyclotron harmonics on the fast-Alfvén branch. The spatiotemporal fast Fourier transform of the perturbed magnetic field $\delta B_z(x,t)$ calculated over the whole grid and simulation duration provides the 2D dispersion relation $\delta B_z(k,\omega)$ where k and ω are the wavenumber and frequency. One-dimensional power spectra are obtained by summing over wavenumber-space. The power spectra consist of 900 points spanning the first 15 hydrogen harmonics.

III. A MODEL FOR FINDING PROBABILITIES OF ICE EMISSION IN VELOCITY SPACE

The relation between the signal $\boldsymbol{s} \in \mathbb{R}^m$ as measured by a given diagnostic and the corresponding velocity distribution $\boldsymbol{f} \in \mathbb{R}^n$ in velocity-space tomography is typically modelled as the matrix-vector equation

$$\boldsymbol{W}\boldsymbol{f} = \boldsymbol{s}^{\mathrm{exact}} + \mathbf{e} \tag{2}$$

for a weight function matrix $\boldsymbol{W} \in \mathbb{R}^{m\times n}$ unique for the diagnostic and Gaussian white noise vector $\mathbf{e}$. The signal vector $\boldsymbol{s}^{\mathrm{exact}}$ is the true signal, and $\boldsymbol{s} = \boldsymbol{s}^{\mathrm{exact}} + \mathbf{e}$ the measured signal including noise. The weight function matrix contains the sensitivities of the diagnostic in velocity space for every measured data point.

Previous work on ICE weight functions computed the 1D weight functions to find the location of the source of the ICE described by the velocity distribution function $\boldsymbol{f} = f(v_\perp)$ from ICE signals by solving the inverse problem in Eq. (2)[51]. It has since been shown that the ICE signal can be Doppler-shifted due to the parallel velocities of the ions[67]. Hence, we here include the parallel velocities and compute the 2D weight functions used to obtain the locations of the ions generating the ICE in velocity space under the same conditions.

A. The inverse problem for ICE

Typically, velocity-space tomography is viewed as the inference of a 2D velocity distribution function $\boldsymbol{f}$ from a signal $\boldsymbol{s}$. For example, consider a Maxwellian distribution $\boldsymbol{f}$. The noise free signal of the diagnostic is then $\boldsymbol{s} = \boldsymbol{W}\boldsymbol{f}$. However, a Maxwellian distribution has no inverted velocity-space gradients or anisotropy, so it will not generate an ICE signal. ICE requires a highly non-Maxwellian subpopulation often modelled as a cold ring distribution $f_{\mathrm{CR}}(v_\parallel, v_\perp) = n_{\mathrm{H}}\delta\left(v_\parallel - u_\parallel\right)\delta\left(v_\perp - u_\perp\right)$ corresponding to a single point in velocity space[70]. The goal of ICE reconstructions is to infer the location of the ICE-generating cold ring distribution from the ICE signal and not the entire fast-ion velocity distribution function.

The probability density function $p\left(v_\parallel, v_\perp \mid p_{\boldsymbol{s}}(\omega)\right)$ of the velocities of the ICE-generating ions with velocity components $(v_\parallel, v_\perp)$ is related to the probability that the source of the ICE occupied a given location in velocity space at the time of emission. The latter probability is contained in the ICE probability density function $p_{\boldsymbol{s}}(\omega)$. Thus, the question becomes: given a measured ICE signal $p_{\boldsymbol{s}}(\omega)$, what is the probability that $p_{\boldsymbol{s}}(\omega)$ originated from certain $v_\parallel$ and $v_\perp$?

From Bayes' theorem, the probability density function $p\left(v_\parallel, v_\perp \mid p_{\boldsymbol{s}}(\omega)\right)$ satisfies

$$p\left(v_\parallel, v_\perp \mid p_{\boldsymbol{s}}(\omega)\right) = \frac{p\left(p_{\boldsymbol{s}}(\omega) \mid v_\parallel, v_\perp\right) p\left(v_\parallel, v_\perp\right)}{p\left(p_{\boldsymbol{s}}(\omega)\right)}, \tag{3}$$

where $\mid$ means 'given'. The sought quantity is the posterior $p\left(v_\parallel, v_\perp \mid p_{\boldsymbol{s}}(\omega)\right)$ giving the probability of the source loca-

tion being at the coordinates $(v_\parallel, v_\perp)$ given the measured signal $p_{\boldsymbol{s}}(\omega)$. This, in turn, is given by the product of the likelihood $p\left(p_{\boldsymbol{s}}(\omega) \mid v_\parallel, v_\perp\right)$ and the prior $p\left(v_\parallel, v_\perp\right)$. The likelihood states the probability of observing such a signal $p_{\boldsymbol{s}}(\omega)$ given the signal originated from ions at $(v_\parallel, v_\perp)$. The prior states the probability of the signal being generated from this location in velocity space before having any measurements (our prior belief). The occurrence of a specific event given a point estimate of $v_\parallel$ and $v_\perp$ is obtained by maximizing the posterior $p\left(v_\parallel, v_\perp \mid p_{\boldsymbol{s}}(\omega)\right)$ as determined by maximum a posteriori (MAP) estimation. Thus,

$$\max_{v_\parallel, v_\perp} p\left(v_\parallel, v_\perp \mid p_{\boldsymbol{s}}(\omega)\right) = \max_{v_\parallel, v_\perp} \frac{p\left(p_{\boldsymbol{s}}(\omega) \mid v_\parallel, v_\perp\right) p\left(v_\parallel, v_\perp\right)}{p\left(p_{\boldsymbol{s}}(\omega)\right)}. \tag{4}$$

Let $\boldsymbol{f}$ be the vector containing the locations of the ions generating the ICE in velocity space, i.e., a 1D array reshaped from the 2D velocity distribution of the ions generating the ICE, and $\boldsymbol{s}$ the measured ICE signal. Furthermore, assume the noise in $\boldsymbol{s}$ is independent and normally distributed. Based on the forward model $\boldsymbol{W}\boldsymbol{f} = \boldsymbol{s}$, the likelihood then satisfies

$$p\left(p_{\boldsymbol{s}}(\omega) \mid v_\parallel, v_\perp\right) \propto \exp\left(-\frac{1}{2}\left\|\boldsymbol{W}\boldsymbol{f} - \boldsymbol{s}\right\|_2^2\right). \tag{5}$$

Suppose the prior follows a multivariate Gaussian distribution, so

$$p\left(v_\parallel, v_\perp\right) \propto \exp\left(-\frac{1}{2}\lambda \left\|\boldsymbol{f}\right\|_2^2\right), \tag{6}$$

where $\lambda > 0$ is a width-scaling for the distribution. Substituting Eqs. (5) and (6) in Eq. (4), we obtain

$$\max_{v_\parallel, v_\perp} p\left(v_\parallel, v_\perp \mid p_{\boldsymbol{s}}(\omega)\right) \propto \max_{\boldsymbol{f}} \left[\exp\left(-\frac{1}{2}\left\|\boldsymbol{W}\boldsymbol{f} - \boldsymbol{s}\right\|_2^2 - \frac{1}{2}\lambda \left\|\boldsymbol{f}\right\|_2^2\right)\right] \tag{7}$$

Since the maximum is attained if and only if the negative logarithm is minimized, we may write

$$\max_{v_\parallel, v_\perp} p\left(v_\parallel, v_\perp \mid p_{\boldsymbol{s}}(\omega)\right) = \min_{v_\parallel, v_\perp} \left\{-\log\left(p\left(p_{\boldsymbol{s}}(\omega) \mid v_\parallel, v_\perp\right)\right) - \log\left(p\left(v_\parallel, v_\perp\right)\right)\right\} \tag{8}$$

$$\Leftrightarrow$$

$$\max_{v_\parallel, v_\perp} p\left(v_\parallel, v_\perp \mid p_{\boldsymbol{s}}(\omega)\right) = \min_{\boldsymbol{f}} \left\{\frac{1}{2}\left\|\boldsymbol{W}\boldsymbol{f} - \boldsymbol{s}\right\|_2^2 + \frac{1}{2}\lambda \left\|\boldsymbol{f}\right\|_2^2\right\}. \tag{9}$$

Equation (9) is the 0th-order Tikhonov regularization formulation used to great success in computing the 2D velocity distributions for the diagnostics mentioned in the introduction. Thus, the interpretation of the velocity distribution of the ions generating the ICE as a probability density function $p\left(v_\parallel, v_\perp \mid p_{\boldsymbol{s}}(\omega)\right)$ given the ICE emission probability density function $p_{\boldsymbol{s}}(\omega)$ is equivalent to solving the equation $\boldsymbol{W}\boldsymbol{f} = \boldsymbol{s}$ using 0th-order Tikhonov regularization.

IV. 2D ICE WEIGHT FUNCTIONS

The physics relating an ICE signal to the location of its driving source in 2D velocity space is contained in the weight function matrix $\boldsymbol{W}$. The weight function matrix is obtained by computing 1D power spectra for a range of $v_\parallel$ and $v_\perp$ which are then subsequently combined appropriately as explained in this section. Recall that a power spectrum contains the signal intensities for all frequencies for a given $v_\parallel$ and $v_\perp$. Collecting the power spectra from low to high $v_\perp$ for a given $v_\parallel$ produces a set of 1D weight function as illustrated in Fig. 1 for $v_\parallel = 0\, v_{\mathrm{A}}$ computed for an ICE detector at LHD, as was done in previous work[51]. The 1D weight functions provide the detector sensitivity at a given frequency for a given parallel velocity, which was assumed to be zero.

To obtain the weight function matrix to be used for reconstructions, the power spectra are stacked as shown in Fig. 2. The result is the matrix W_{ijk}. The i index corresponds to $v_\parallel$, the j index to $v_\perp$, and the k index to ω (not to be confused with the wavenumber k). Cross-sections across the frequency dimension of W_{ijk} result in 2D weight functions in $v_\parallel$ and $v_\perp$. The dashed line in Fig. 2 indicates a cross-section of the 3D array for $v_\parallel = 0\, v_{\mathrm{A}}$, showing the 1D power spectrum from Fig. 1. The horizontal cross sections are the 2D weight functions.

The $v_\parallel$-resolution is $0.1\, v_{\mathrm{A}}$, and the frequency resolution is $\Omega_{\mathrm{H}}/60 \approx 0.6$ MHz. The frequency range of ω is 0 to 15 Ω_{H}, where Ω_{H} is the fundamental hydrogen cyclotron frequency. This frequency range equals that used in prior work on ICE weight functions[51]. Each signal peak around the harmonics contains around 10-15 frequency measurements corresponding to $6-9$ MHz.

V. CHARACTERISTICS OF 2D ICE WEIGHT FUNCTIONS IN $v_\parallel$ AND $v_\perp$

In this section we discuss the characteristics of the 2D ICE weight function formalism to infer the probability density function of the ICE-generating ions in velocity space. This development includes analysis of the characteristics of the 2D ICE weight functions in the spectral vicinity of harmonics and for increasing harmonic number.

Fig. 3 shows the 2D ICE weight functions at several frequencies close to the fourth harmonic. ICE weight functions

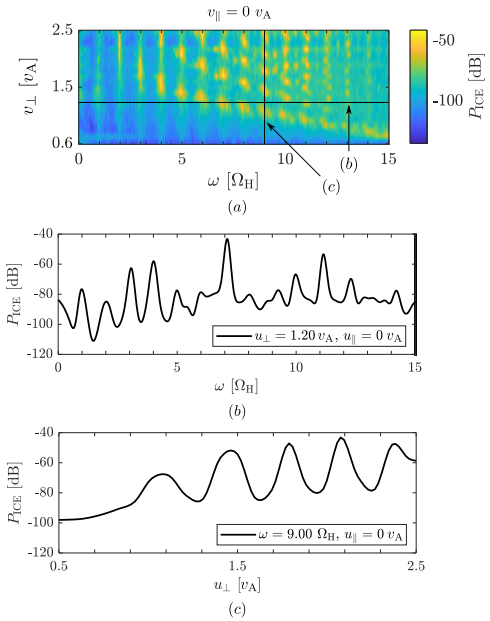

FIG. 1. (a) Power spectra computed for $v_\parallel = 0\ v_A$ and $v_\perp \in [0.6, 2.6]$ v_A and combined into one figure computed for an MCI at LHD. (b) An example power spectrum for $v_\perp = 1.20\ v_A$ and $v_\parallel = 0\ v_A$. (c) A 1D weight function in $v_\perp$ for $v_\parallel = 0\ v_A$.

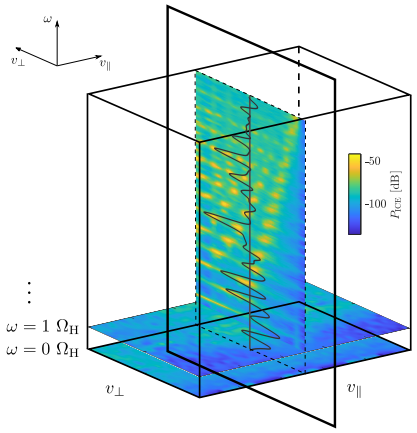

FIG. 2. The 3D weight function matrix W_{ijk} is obtained by stacking the 1D power spectra according to the location of the ring distribution $f(v_\parallel, v_\perp)$. The intersection of the black square with the cube indicated by a dashed line is a cross section of the 3D matrix at a specific $v_\parallel$. Each vertical line corresponds to a power spectrum, as indicated by the vertical central line.

quantify the expected signal given an ion at a location $(v_\parallel, v_\perp)$. The high-sensitivity areas occur in bands wide in $v_\parallel$ and narrow in $v_\perp$. At 3.83 Ω_H, the sensitivity is largest for positive $v_\parallel$. The closer the frequency is to the fourth harmonic, the smaller $v_\parallel$ of the most sensitive region, until right at the fourth harmonic where the sensitivity is largest for $v_\parallel = 0$. The same pattern is seen for frequencies larger than the fourth harmonic, where $v_\parallel$ of the most sensitive region increases in the negative direction with the frequency shift. This is due to the Doppler shift term $k_\parallel v_\parallel$ in the resonance condition

$$\omega = n\Omega_H + k_\parallel v_\parallel. \tag{10}$$

The sensitivity patterns illustrated in Fig. 3 occur for every harmonic. Fig. 4 illustrates examples of higher harmonics. For $v_\perp \in [0.6\,v_A, 2.6\,v_A]$, the number of high-sensitivity bands increases by 1 every second harmonic with no high-sensitivity band occurring at the first harmonic. Thus, for lower frequencies, only specific $v_\perp$ can contribute to the signal generation. For higher frequencies, several bands in $v_\parallel$ with different values of $v_\perp$ can contribute to the signal generation. Further, the width of the bands decreases with increasing harmonic number, and they occur for lower values of $v_\perp$.

VI. INVERSION METHODS FOR ICE

The goal of ICE reconstructions is to infer the velocity-space location of the ICE-generating ions from an ICE signal. This is achieved by solving the inverse problem in $\boldsymbol{W}\boldsymbol{f} = \boldsymbol{s}$, and the resulting 2D probability distribution of the location of ICE emission $\boldsymbol{f}$ is called a 'reconstruction'. A regular least-square inversion fails since the problem is ill-posed. Here, we illustrate three different techniques to compute reconstructions: (i) 0th-order Tikhonov regularization, (ii) a least-square subset search, and (iii) Lasso regularization. In the following, we consider values of $v_\parallel \in [-2.6\,v_A, 2.6\,v_A]$ and $v_\perp \in [0.6\,v_A, 2.6\,v_A]$. The grid discretizes velocity space into single pixels of size approximately 0.1 $v_A \times 0.1\ v_A$. To avoid performing inverse crime when reconstructing the 2D velocity-space distributions of the ICE-generating ions, a finer grid is used to create the ICE signals in the forward model; see Ref [80] p. 139 ff. for details. This grid is five times as fine, i.e., 0.02 $v_A \times 0.02\ v_A$.

In the following calculations, it is assumed that ICE is likely to be generated at only one or a few locations in velocity space. This is well motivated, as current theory suggests the primary generation mechanism of ICE is given by a cold ring distribution[84], cf. the discussion in Section II.

A. Tikhonov regularization

As shown above in Eq. (9), 0th-order Tikhonov regularization solves the problem

$$\boldsymbol{f}^* = \underset{\boldsymbol{f}}{\operatorname{argmin}} \|\boldsymbol{W}\boldsymbol{f} - \boldsymbol{s}\|_2^2 + \lambda \|\boldsymbol{f}\|_2^2 \tag{11}$$

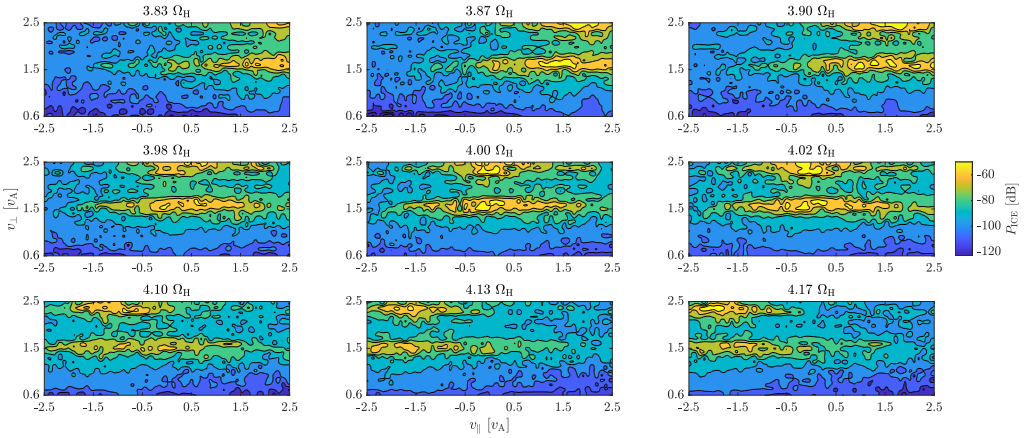

FIG. 3. 2D weight functions in $v_\parallel$ and $v_\perp$ around the fourth hydrogen harmonic. The high-sensitivity regions are indicated by a bright yellow colour. Note the movement of the center of the highest sensitivity region for $v_\perp \approx 1.5\ v_\mathrm{A}$ from around $v_\parallel \approx 2.0 v_\mathrm{A}$ at $3.83\Omega_\mathrm{H}$ to $v_\parallel = 0\, v_\mathrm{A}$ at $4\,\Omega_\mathrm{H}$ to $v_\parallel \approx -1.5\, v_\mathrm{A}$ at $4.17\,\Omega_\mathrm{H}$. Note also how the second band occurs for progressively lower $v_\perp$ as the frequency increases.

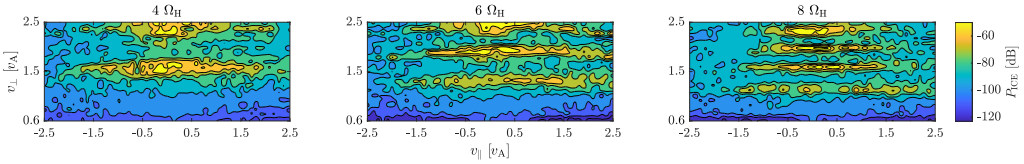

FIG. 4. 2D weight functions for the $\omega = 4\ \Omega_\mathrm{H}, 6\ \Omega_\mathrm{H}$, and $8\ \Omega_\mathrm{H}$. Note that the number of sensitivity bands increases by one every second harmonics. The width of the bands in $v_\perp$ decrease for higher harmonics.

for some non-negative value of the regularization parameter λ, where the factors of $1/2$ have been removed. The noise e in the measured signal $\boldsymbol{s} = \boldsymbol{s}^\mathrm{exact} + e$ influences the accuracy of the reconstruction $\boldsymbol{f}^*$. The weight function matrix $\boldsymbol{W}$ determines how much the noise affects the reconstruction. An upper bound on the error in the reconstruction is

$$\frac{\|\delta \boldsymbol{f}\|_2}{\|\boldsymbol{f}\|_2} \leq \kappa(\boldsymbol{W}) \frac{\|\delta \boldsymbol{s}\|_2}{\|\boldsymbol{s}\|_2}, \tag{12}$$

where $\kappa(\boldsymbol{W}) = s_1/s_n$ is the condition number defined in terms of the largest and smallest singular values s_1 and s_n of $\boldsymbol{W}$. For our weight function matrix, $\kappa(\boldsymbol{W}) \approx 10^4$, so the problem is not well-conditioned, but it is also not terribly ill-conditioned. For other inverse problems such as velocity-space tomography of CTS or FIDA signals, $\kappa(\boldsymbol{W}) > 10^{15}$ indicating a significant need for regularization. However, in the case of ICE generated by an MCI at LHD, observation-relevant noise levels of around 10% might not impact the reconstruction $\boldsymbol{f}^*$ to a significant degree due to the relatively low value of $\kappa(\boldsymbol{W})$. The insignificant influence of the noise in the reconstruction is reflected in some synthetic signals having $\lambda \approx 10^{-7}$ as the optimal regularization parameter.

Characteristics of the solution are reflected in the singular vectors $\boldsymbol{v}_i$ of the singular value decomposition (SVD) of $\boldsymbol{W}$[85]. For any matrix $\boldsymbol{W} \in \mathbb{R}^{m\times n}$, the SVD can be written as

$$\boldsymbol{W} = \boldsymbol{U}\boldsymbol{\Sigma}\boldsymbol{V}^T = \sum_{i=1}^{r} \boldsymbol{u}_i \sigma_i \boldsymbol{v}_i^T, \tag{13}$$

where $r \leq \min(m,n)$ is the rank of $\boldsymbol{W}$, $\boldsymbol{U} \in \mathbb{R}^{m\times m}$ and $\boldsymbol{V} \in \mathbb{R}^{n\times n}$ are unitary matrices, and $\boldsymbol{\Sigma} \in \mathbb{R}^{m\times n}$ is a rectangular matrix with positive real numbers σ_i, $i = 1,\ldots,r$, on the diagonal $(m = n)$. These numbers, called the 'singular values', satisfy $\sigma_1 \geq \sigma_2 \geq \cdots \geq \sigma_r$. The matrices $\boldsymbol{U}$ and $\boldsymbol{V}$ contain the left and right singular vectors,

$$\boldsymbol{U} = (\boldsymbol{u}_1, \boldsymbol{u}_2, \ldots, \boldsymbol{u}_m), \quad \boldsymbol{V} = (\boldsymbol{v}_1, \boldsymbol{v}_2, \ldots, \boldsymbol{v}_n). \tag{14}$$

Without any regularization, the naïve solution to Eq. (2) can be written in terms of the SVD components as

$$\boldsymbol{f} = \boldsymbol{W}^\dagger \boldsymbol{s} = \sum_{i=1}^{n} \frac{\boldsymbol{u}_i^T \boldsymbol{s}}{\sigma_i} \boldsymbol{v}_i, \tag{15}$$

where $\boldsymbol{W}^\dagger$ is the Moore-Penrose pseudo-inverse of $\boldsymbol{W}$. Several regularization methods can be written as a filtered SVD

expansion of the form

$$\boldsymbol{f}_{\mathrm{reg}} = \sum_{i=1}^{n} \varphi_i \frac{\boldsymbol{u}_i^T \boldsymbol{s}}{\sigma_i} \boldsymbol{v}_i, \tag{16}$$

where φ_i are the filter factors of the given regularization method. For 0th-order Tikhonov regularization, the filter factors in terms of the regularization parameter λ are

$$\varphi_i^{[\lambda]} = \frac{\sigma_i^2}{\sigma_i^2 + \lambda^2} \approx \begin{cases} 1, & \text{for } \sigma_i \gg \lambda, \\ \sigma_i^2/\lambda^2, & \text{for } \sigma_i \ll \lambda. \end{cases} \tag{17}$$

Thus, for all i such that the singular values σ_i are larger than λ, the SVD components contribute almost fully to the solution. For all i such that the singular values σ_i are much smaller than λ, the SVD components are damped and do not contribute as much to the solution. Hence, the right singular vectors $\boldsymbol{v}_i$ corresponding to the largest singular values contribute the most to a Tikhonov-regularized solution. The characteristics of these vectors will therefore be reflected in the solutions found.

The first nine right singular vectors are shown in Fig. 5. Observe that the first five have areas spanning a wide range of $v_\parallel$ and $v_\perp$ with approximately equal intensity within the given range. The right singular vectors numbered six to nine have clear bands in the $v_\parallel$ direction for a small range of $v_\perp$. These properties indicate that the sensitivity in $v_\perp$ is good and the sensitivity in $v_\parallel$ worse. Thus, we expect to do better in finding the location of the ICE-generating ions in the $v_\perp$-direction than in the $v_\parallel$-direction.

B. The least-square subset search

Since we are looking for a particular location in velocity space rather than for an entire distribution function, it might be feasible to simply compare synthetic data from all possible locations in velocity space with the actual data. For ICE-generating ions at any location in velocity space, we can calculate the corresponding ICE signal using the forward model in Eq. (2). Thus, we compute a signal $\boldsymbol{\sigma}^{[i]}$ for every possible location of ICE emission in velocity space $\boldsymbol{\varphi}^{[i]}$ (not to be confused with the singular values and filter factors defined above) and store it in an array $D_\sigma = [\boldsymbol{\sigma}^{[1]}, \ldots, \boldsymbol{\sigma}^{[N]}]$, where the superscript '$[i]$' indicates the number in the array, while also storing the corresponding velocity distributions in the array $D_\varphi = [\boldsymbol{\varphi}^{[1]}, \ldots, \boldsymbol{\varphi}^{[N]}]$. The number N is the total number of simulated ICE signals and velocity distributions. The elements in the arrays satisfy $\boldsymbol{W}\boldsymbol{\varphi}^{[i]} = \boldsymbol{\sigma}^{[i]}$.

Consider then the subset $V \subseteq D_\varphi \oplus D_\sigma$ consisting of all physically relevant $(\boldsymbol{\sigma}^{[i]}, \boldsymbol{\varphi}^{[i]})$-pairs. A measured ICE signal $\boldsymbol{s} = \boldsymbol{s}^{\mathrm{exact}} + e$ consisting of the underlying exact signal $\boldsymbol{s}^{\mathrm{exact}}$ and noise vector e being additive white and Gaussian with $e \sim \mathcal{N}(0, \eta^2 I)$ is then compared against the first entry of all elements in V by calculating

$$\Delta_2(\boldsymbol{s}, \boldsymbol{\sigma}^{[i]}) \equiv \left\| \boldsymbol{s} - \boldsymbol{\sigma}^{[i]} \right\|_2^2 \tag{18}$$

for all i. The signal $\boldsymbol{\sigma}^{*[i]}$ with lowest Δ_2 is chosen to be $\boldsymbol{s}^{\mathrm{exact}}$. The corresponding distribution $\boldsymbol{\varphi}^{*[i]}$ used to generate $\boldsymbol{\sigma}^{*[i]}$ is then considered to contain the location of the ions that generated the signal. If the exact signal is not in the subset, the closest match is chosen by minimizing Δ_2.

Several challenges are associated with this technique: (i) the noise e may corrupt the measured signal $\boldsymbol{s}$ so the best-fitting signal $\boldsymbol{\sigma}^{*[i]}$ suggested by the least-square subset search is incorrect, (ii) if ICE originates from more than one location, the subset may be too large to be stored on a server, and (iii) computations may take too long due to the large size of the subset. We suggest ways to overcome these challenges below.

For the least-square subset search, it is impractical to assign locations in velocity space continuous probabilities. Thus, we need only consider a subset. Since the primary goal of ICE reconstructions is to infer the location of the ions generating the ICE in velocity space, we may assume that the values of a pixel are binary: '0' indicates that no part of the ICE signal was generated from this location in velocity space, and '1' indicates that this location of velocity space generated part of or all of the ICE signal.

To avoid dependency of the synthetic ICE signals $\boldsymbol{\sigma}^{[i]}$ and measured ICE signals $\boldsymbol{s}$ on the intensity of the pixels in discretized velocity space, $\boldsymbol{\sigma}^{[i]}$ and $\boldsymbol{s}$ are normalized before being stored. This also removes any experimental calibration errors. Thus, in the synthetic data generation, a power spectrum $\boldsymbol{\sigma}^{[i]} = \boldsymbol{W}\boldsymbol{\varphi}^{[i]}$ is first generated using the fine discretization of velocity space, then noise added, and the spectrum normalized.

C. Lasso regularization

Letting the regularization term in Eq. (9) be the one-norm instead of the Euclidean norm, we obtain the so-called 'Lasso' regularization[86],

$$\boldsymbol{f}^* = \underset{\boldsymbol{f}}{\operatorname{argmin}} \|\boldsymbol{W}\boldsymbol{f} - \boldsymbol{s}\|_2^2 + \lambda \|\boldsymbol{f}\|_1. \tag{19}$$

Note that Eq. (19) is a MAP estimate with a Laplace prior on $\boldsymbol{f}$, so the model for finding probabilities of ICE emission in velocity space derived in Section III holds. If the regularization parameter λ is sufficiently large, some of the entries in $\boldsymbol{f}$ are driven to zero. Thus, the Lasso regularization promotes sparsity in the solution. This is especially desirable when reconstructing ICE-generating distributions localized to a single pixel. This regularization method sometimes avoids the jitter in the Tikhonov-regularized solutions, as shown below. Lasso-regularized solutions are determined using the implementation of Lasso in MATLAB.

VII. RECONSTRUCTIONS OF THE LOCATIONS OF THE IONS GENERATING THE ICE IN VELOCITY SPACE

To generate the arrays for one ring beam least-square subset searches, a single non-zero pixel with a value of 1 was placed at each grid point in velocity space. The corresponding signal was then generated by computing $\boldsymbol{W}\boldsymbol{\varphi}^{[i]} = \boldsymbol{\sigma}^{[i]}$ and the normalized $\boldsymbol{\varphi}^{[i]}$ and $\boldsymbol{\sigma}^{[i]}$ stored in D_φ and D_σ.

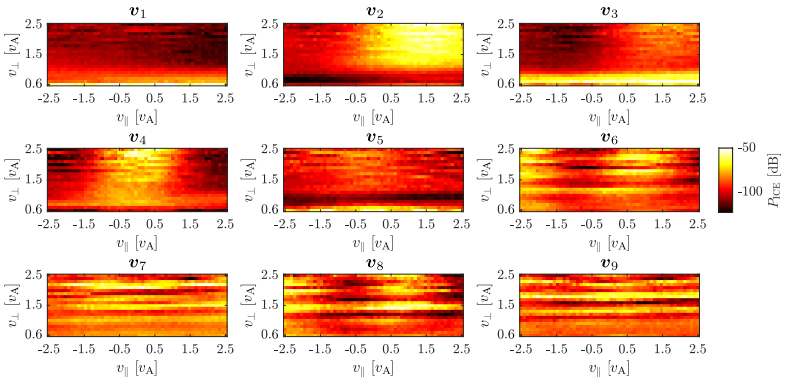

FIG. 5. The first nine right singular vectors $\boldsymbol{v}_i$ from the SVD of $\boldsymbol{W}$. They reflect the dominant components of the regularized solution found using Tikhonov regularization. Observe the large areas with the same sensitivity for the first five vectors and the bands in the $v_\parallel$-direction for the singular vectors numbered six to nine. These properties reflect the sensitivity of the regularized solutions in $v_\parallel$ and $v_\perp$.

We want to determine how well the least-square subset search, Tikhonov regularization, and Lasso regularization can reconstruct a given one ring beam distribution for a synthetic ICE signal with 10% noise. The reconstructions found by the three different techniques are compared to the ground truth source location of ICE emission. Further, they are multiplied with $\boldsymbol{W}$ to obtain the signal for the reconstructed solution to locate deviations from the noise-free signal corresponding to the ground truth distribution.

We begin by considering a velocity distribution consisting of a single pixel in velocity space; see the first row in Fig. 6 for an example of a ground truth and the corresponding ICE signal. Ten percent noise is added to the ICE signal. The three techniques are then used to determine the locations of the ions generating the ICE in velocity space.

From the ICE signal with added noise, the least-square subset search is able to perfectly reconstruct the ground truth; see the second row in Fig. 6. The small differences in the database solution compared to the ground truth occur due to the different grid sizes used to generate the signals in the database compared to the grid used to generate the ground truth signal to avoid performing inverse crime.

The optimal reconstruction from 0th-order Tikhonov regularization is also close to the ground truth distribution. A few non-zero pixels with low intensities adjacent to the correct location in velocity space which should not be a part of the velocity distribution occur. However, the correct location of the ground truth distribution is found and clearly indicated in the figure by the high-intensity pixel; see the third row of Fig. 6. The occurrence of a number of pixels with low intensities, which we call 'jitter', occurs for all ICE Tikhonov reconstructions to a smaller or larger degree. The amount of jitter depends on the complexity of the ground truth distribution as demonstrated below. However, as is clear from Fig. 6, the signal corresponding to the reconstruction found using Tikhonov regularization is almost identical to the ground truth.

The optimal reconstruction using Lasso regularization is quite similar to the Tikhonov or the least-square subset reconstructions: for a sufficiently large value of λ, only the true location in the velocity distribution remains. However, it is clear that the Lasso solution is more sparse than the Tikhonov solution.

A. Noise investigation

Two investigations were performed to identify the impact of different noise levels in the signal on the accuracy of the reconstructions: for a ring distribution of size 0.5×0.2 v_A, (i) 0th-order Tikhonov regularization and Lasso regularization were performed for the corresponding ICE signal with 1-10% noise added, and (ii) reconstructions with all three methods for 0-100% noise added; see Figs. 7 and 8.

Fig. 7 shows the investigated ground truth signal and the Δ_2 value for Tikhonov regularization, the subset search, and Lasso regularization as a function of the noise percentage. The subset D_φ consists in this case of every one ring distribution in velocity space with size 0.5×0.2 v_A. The subset search is the preferred reconstruction method up to around 60% noise, where it then remains on par with Tikhonov regularization. The correct central locations are found by the subset search for at least up to 10% noise. The best reconstructions found using Tikhonov and Lasso regularization for 1-5% noise compare to the reconstruction found using the subset search with around 30% noise.

As shown in Fig. 8, close to perfect reconstructions with a small amount of jitter are found for the lowest levels of noise, whereas more jitter occurs for 10% noise, indicating a larger

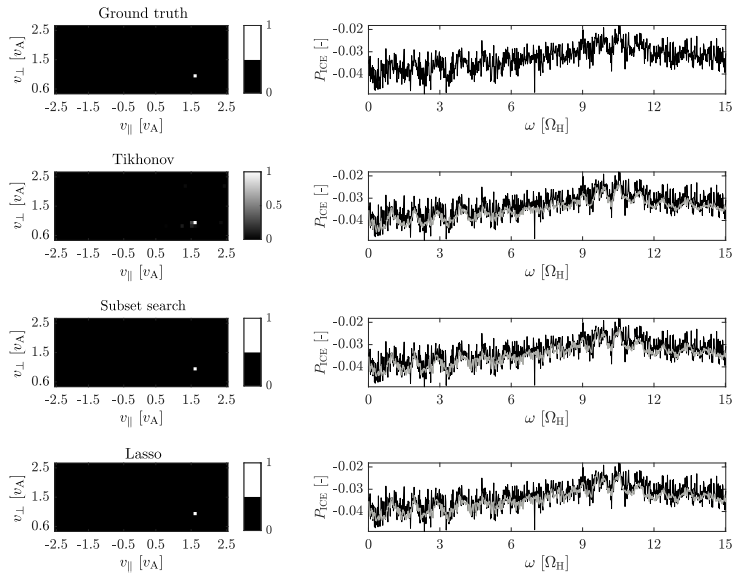

FIG. 6. The velocity-space distribution of ICE-generating ions shown to the left in the first row was used to generate the ICE signal to its right. The same signal with 10% noise was then used to compute the reconstructions using the least-square subset search (second row), 0th-order Tikhonov regularization (third row), and Lasso regularization (fourth row). The signals for the three different techniques are plotted in the second column as a grey signal on top of the black ground truth signal.

FIG. 7. The least-square subset search is superior to Tikhonov and Lasso regularization for up to around 60% noise and is able to find the exact locations of the ions generating the ICE for at least up to 10% noise in the ICE signal. The reconstructions found using 0th-order Tikhonov regularization and Lasso regularization are almost identical up to 30% noise as indicated by the almost identical value of Δ_2 for 0-30% noise. Lasso regularization remains the worst technique for all other noise levels.

uncertainty of the extent of the velocity distribution. Note that only Tikhonov solutions are shown, as the Lasso solutions are almost identical; see also the Δ_2 values for both methods in Fig. 7. The jitter is mostly spread in $v_\parallel$, which is in line with the interpretation from the SVD; see Fig. 5. The central location of the distribution in velocity space is clear for all noise levels in the range of 1-10% indicated by the highest intensity pixels.

B. Reconstructions of Gaussian distributions in $v_\parallel$ and $v_\perp$

A natural follow-up to the above investigations is how well distributions with shapes other than rectangular and no longer binary but with values in the interval $[0,1]$ can be reconstructed by the subset search, Tikhonov regularization, and Lasso regularization. Here, we consider distributions with Gaussian blobs specified by a central location $(\mu_{v_\parallel}, \mu_{v_\perp})$ in velocity space and the standard deviations $\sigma_{v_\parallel}$ and $\sigma_{v_\perp}$. Further, the quality of the reconstructions from each method for Gaussian distributions indicates the quality of reconstructions of other shapes.

The Gaussian blob shown in Fig. 9 has standard deviations of $\sigma_{v_\parallel} = 0.2\,v_A$ and $\sigma_{v_\perp} = 0.1\,v_A$. A 1-pixel subset search can identify the central location of a single Gaussian distribution; see the top row in Fig. 9. The subset search can identify the correct central location for such a distribution anywhere in velocity space. Also, the distribution can be of any size, and the subset search correctly finds the location in velocity space. A solution found using Tikhonov regularization produces results

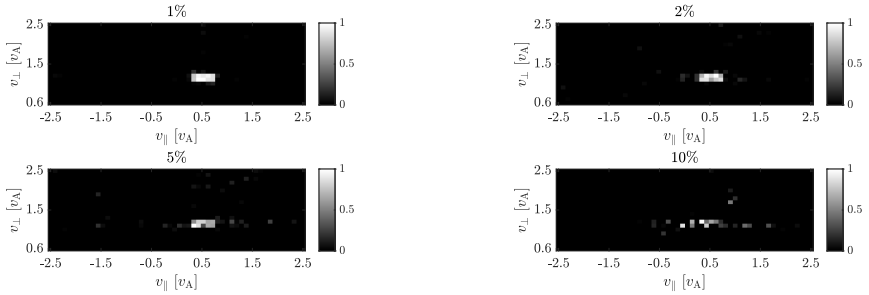

FIG. 8. The reconstructions from the ground truth ICE emission location shown in Fig. 7 using 0th-order Tikhonov regularization as a function of the noise percentage in the signal (1-10%). Lasso regularization produces almost identical reconstructions and are therefore not illustrated.

similar to those shown above for rectangular signals; see the middle row of Fig. 9. In the Tikhonov solution, the highest intensity pixels are located at the central locations of the Gaussian blob with jitter mostly within the original distribution. The dominant error in the solution is in the $v_\parallel$ direction as predicted from the SVD; see Fig. 5. The same conclusions hold for the solution found using Lasso regularization. In conclusion, all three techniques successfully identify the location of the ions generating the ICE in all velocity space for a single Gaussian blob of any size.

We conclude that the solutions from the subset search, Tikhonov regularization, and Lasso regularization behave similarly, independent of the shape of the velocity-space distributions of the ions generating the ICE: the subset search finds the pixel at the central locations of the distributions, and similarly for Tikhonov regularization and Lasso regularization but with small amounts of erroneously placed jitter.

VIII. DISCUSSION AND CONCLUSION

Prior work has computed and validated the weight functions needed to reconstruct the 2D fast-ion velocity distribution function for measurements from diagnostics such as CTS, FIDA, GRS, NES, and FILDs. However, the recently developed weight functions and reconstructions for ICE were limited to 1D in $v_\perp$, assuming $v_\parallel = 0$.

In this study, we computed the 2D weight functions for edge ICE caused by the MCI for conditions at LHD using a nonlinear 1D3V PIC-hybrid code. We compute power spectra for a specific value of $v_\parallel$ in the range -2.6 to 2.6 v_A and $v_\perp$ in the range 0.6 to 2.6 v_A. In the simulations, we assume emission from one radial location (slab geometry and no gradients in B, n_e, and T_e), from one wavevector direction, and no detector response functions while still retaining the full interaction between the fields and the kinetic ions. The weight functions are obtained by stacking the power spectra appropriately to obtain ascending values of $v_\perp$ and $v_\parallel$ in the first and second dimensions and the angular frequency ω in the third dimension. The result is a 3D array with 2D weight functions for every frequency.

The weight functions exhibit a particular pattern for frequencies close to the cyclotron harmonics. For frequencies below the harmonics, the highest signal sensitivities occur for positive $v_\parallel$. Conversely, for frequencies above the harmonics, the highest signal intensities occur for negative $v_\parallel$. At the frequency of the harmonic, ions with $v_\parallel = 0$ have the highest sensitivity. This effect is due to the Doppler shift. Also, the sensitivities occur in horizontal bands in $v_\perp$ so only some specific values of $v_\perp$ contribute to the measured signal. Tikhonov and Lasso-regularized reconstructions have good resolution in $v_\perp$ for this reason.

Reconstructions can be performed for synthetic velocity distributions for the ions generating the ICE using a least-square subset search, 0th-order Tikhonov regularization, and Lasso regularization for noise realizations at least up to 10%. The least-square subset search is able to correctly identify the central locations of the distributions independent of the level of noise added, but the drawback is the requirement of large storage space if the subset is to consist of anything but single-pixel functions generating the ICE.

Tikhonov and Lasso reconstructions are accurate for localized distributions in velocity space. With increasing size of the distributions, the reconstructions are corrupted by erroneous jitter occurring at incorrect locations in velocity space. Still, Tikhonov and Lasso reconstructions have high resolution in $v_\perp$ and contain high-intensity pixels in the signal locations of the distributions in velocity space.

We performed our simulations for edge ICE at LHD. Thus, extending the results to other machines requires new simulations to obtain the 2D weight functions. Therefore, future work should investigate whether it is possible to reproduce the results of this study for synthetic ICE signals at other machines. However, this study indicates the feasibility of the ICE diagnostic for use at both current and future machines to diagnose fast-ion behaviour. Thus, our results support the proposal to include the ICE diagnostic at ITER, where it could contribute to integrated data analysis for alpha particle distribution functions[87].

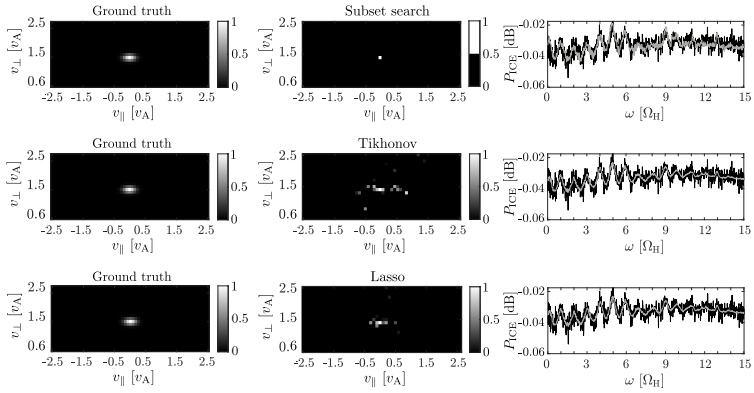

FIG. 9. The subset least-square search (top row), 0th-order Tikhonov regularization (middle row), and Lasso regularization (bottom row) solutions for a Gaussian distribution. The ground truths are shown on the left, the reconstructions in the middle, and the signals for the reconstructions on the right. The subset search finds the correct central location of the Gaussian blob. Tikhonov and Lasso regularization also finds the correct location of the distribution with some jitter.

IX. ACKNOWLEDGEMENTS

This work has been carried out within the framework of the EUROfusion Consortium, funded by the European Union, via the Euratom Research and Training Program (Grant Agreement No. 101052200 - EUROfusion). The views and opinions expressed here are, however, those of the authors only and do not necessarily reflect those of the European Union or the European Commission. Neither the European Union nor the European Commission can be held responsible for them. This work was also supported by the Villum Synergy grant no. VIL50096 from the Villum Foundation. We thank Professor Per Christian Hansen for his contributions.

X. AUTHOR DECLARATIONS

The authors have no conflicts to disclose.

XI. DATA AVAILABILITY STATEMENT

The data that support the findings of this study are available from the corresponding author upon reasonable request.

Appendix A: Code Description

We employed the hybrid particle-in-cell (PIC) simulation code PROMETHEUS++[68] in our simulations. This code incorporates a one-space-dimension and three-velocity-space-dimensions (1D3V) scheme and solves the Vlasov equation for an arbitrary number of ion species. It does this self-consistently with the electric and magnetic fields and an electron fluid.

PROMETHEUS++ calculates and iterates the Lorentz force for an extensive array of macroparticles representing the different ion populations. These iterative calculations offer an effective method to track the dynamic behaviour of the ion species. Simultaneously, the code utilises a fixed grid to compute solutions for Maxwell's equations under the Darwin approximation. This approach maintains the full-ion gyromotion, thus facilitating the study of resonant wave-particle interactions such as ICE in the linear and non-linear phases.

Furthermore, PROMETHEUS++ is capable of simulating a variety of waves. These encompass fluid waves, such as fast Alfvén and whistler waves, and kinetic waves, including ion Bernstein modes and ion cyclotron modes in weakly magnetised plasmas where the cyclotron frequency is significantly smaller than the plasma frequency, i.e., $\Omega_H \ll \omega_p$.

The model is based on quasineutrality, where the electron density n_e equals the summed product of the charge number Z_l and density n_l for each of the N ion species l. This relationship is expressed as

$$n_e = \sum_{l=1}^{N} Z_l n_l. \tag{A1}$$

The kinetic ions in the model are subject to the macroscopic Lorentz force. We represent this by assigning each macroparticle, labelled as p (omitting the species index l for simplicity, and assuming p runs from 1 to N_l), with an ion mass m_p and charge q_p:

$$\begin{aligned} \frac{dx_p}{dt} &= v_p \\ m_p \frac{d\mathbf{v}_p}{dt} &= q_p \left(\mathbf{E} + \mathbf{v}_p \times \mathbf{B}\right) \end{aligned} \tag{A2}$$

Within the model, the ion densities n_l and macroscopic velocities $\mathbf{u}_l$ are deposited on the grid using the cloud-in-cell scheme[88,89].

The model defines the charge-weighted mean ion velocity $\mathbf{V}_i$ as

$$\mathbf{V}_i = \frac{\sum_{l=1}^{N} Z_l n_l \mathbf{u}_l}{\sum_{l=1}^{N} Z_l n_l}. \tag{A3}$$

Next, we consider the massless fluid electron momentum equation, which includes $\mathbf{V}_e$ and T_e - representing the electron bulk velocity and temperature, respectively - and an isothermal pressure law, $p_e = n_e T_e$. From this, we derive the generalised Ohm's law for the electric field $\mathbf{E}$:

$$\frac{\partial}{\partial t} n_e m_e \mathbf{V}_e = -e n_e \left(\mathbf{E} + \mathbf{V}_e \times \mathbf{B}\right) - \nabla p_e, \tag{A4}$$

which simplifies to

$$\mathbf{E} = -\mathbf{V}_e \times \mathbf{B} - \frac{\nabla p_e}{e n_e} \tag{A5}$$

since $\partial n_e m_e \mathbf{V}_e / \partial t = 0$. Furthermore, we observe that $\nabla \cdot \mathbf{B} = 0$ implies that $B_x = 0$, where x represents the distance along the 1D slab-geometry spatial domain. We then use Faraday's law to solve for $\mathbf{B}$:

$$\frac{\partial \mathbf{B}}{\partial t} = -\nabla \times \mathbf{E}. \tag{A6}$$

Simultaneously, we apply Ampère's law within the Darwin approximation[65]:

$$\nabla \times \mathbf{B} = \mu_0 \mathbf{J} = \mu_0 e n_e \left(\mathbf{V}_i - \mathbf{V}_e\right), \tag{A7}$$

which, when combined with the massless electron momentum equation, leads to the generalised Ohm's law expressed in terms of $\mathbf{V}_i$ and $\mathbf{B}$[90], i.e.,

$$\mathbf{E} = -\mathbf{V}_i \times \mathbf{B} + \frac{1}{\mu_0 e n_e} \left(\nabla \times \mathbf{B}\right) \times \mathbf{B} - \frac{\nabla p_e}{e n_e}. \tag{A8}$$

[1] N. A. Crocker, S. X. Tang, K. E. Thome, J. B. Lestz, E. V. Belova, A. Zalzali, R. O. Dendy, W. A. Peebles, K. K. Barada, R. Hong, T. L. Rhodes, G. Wang, L. Zeng, T. A. Carter, G. H. Degrandchamp, W. W. Heidbrink, and R. I. Pinsker, "Novel internal measurements of ion cyclotron frequency range fast-ion driven modes," Nuclear Fusion **62**, 026023 (2022).
[2] R. O. Dendy, C. N. Lashmoredavies, and K. F. Kam, "A possible excitation mechanism for observed superthermal ion-cyclotron emission from tokamak plasmas," Physics of Fluids B-plasma Physics **4**, 3996–4006 (1992).
[3] R. DENDY, "Interpretation of ion-cyclotron emission from fusion and space plasmas," Plasma Physics and Controlled Fusion **36**, B163–B172 (1994).
[4] K. G. Mc Clements, C. Hunt, R. O. Dendy, and G. A. Cottrell, "Ion cyclotron emission from jet d-t plasmas," Physical Review Letters **82**, 2099–2102 (1999).
[5] G. A. Cottrell, V. P. Bhatnagar, O. DaCosta, R. O. Dendy, J. Jacquinot, K. G. McClements, D. C. McCune, M. F. F. Nave, P. Smeulders, and D. F. H. Start, "Ion-cyclotron emission measurements during jet deuterium-tritium experiments," Nuclear Fusion **33**, 1365–1387 (1993).
[6] K. Saito, R. Kumazawa, T. Seki, H. Kasahara, G. Nomura, F. Shimpo, H. Igami, M. Isobe, K. Ogawa, K. Toi, M. Osakabe, M. Nishiura, T. Watanabe, S. Yamamoto, M. Ichimura, and T. Mutoh, "Measurement of ion cyclotron emissions by using high-frequency magnetic probes in the lhd," Plasma Science and Technology **15**, 209–212 (2013).
[7] N. N. Gorelenkov, "Energetic particle-driven compressional alfvén eigenmodes and prospects for ion cyclotron emission studies in fusion plasmas," New Journal of Physics **18**, 105010 (2016).
[8] W. W. Heidbrink, E. D. Fredrickson, N. N. Gorelenkov, T. L. Rhodes, and M. A. Van Zeeland, "Observation of compressional alfvén eigenmodes (cae) in a conventional tokamak," Nuclear Fusion **46**, 324–334 (2006).
[9] E. D. Fredrickson, N. Gorelenkov, C. Z. Cheng, R. Bell, D. Darrow, D. Johnson, S. Kaye, B. LeBlanc, J. Menard, S. Kubota, and W. Peebles, "Observation of compressional alfvén modes during neutral-beam heating on the national spherical torus experiment," Physical Review Letters **87**, 145001 (2001).
[10] L. C. Appel, T. Fülöp, M. J. Hole, H. M. Smith, S. D. Pinches, and R. G. Vann, "Compressional alfvén eigenmodes on mast," Plasma Physics and Controlled Fusion **50**, 115011 (2008).
[11] R. Ochoukov, R. Bilato, V. Bobkov, S. Chapman, R. Dendy, M. Dreval, H. Faugel, A. Kappatou, Y. Kazakov, M. Mantsinen, K. McClements, D. Moseev, S. Nielsen, J. Noterdaeme, M. Salewski, P. Schneider, and M. Weiland, "High frequency alfvén eigenmodes detected with ion-cyclotron-emission diagnostics during nbi and icrf heated plasmas on the asdex upgrade tokamak: Paper," Nuclear Fusion **60**, 126043 (2020).
[12] R. Ochoukov, S. Sipilä, R. Bilato, V. Bobkov, M. Dreval, M. Weiland, R. Dendy, H. Faugel, T. Johnson, A. Kappatou, Y. Kazakov, K. G. McClements, D. Moseev, M. Salewski, and P. Schneider, "Analysis of high frequency alfvén eigenmodes observed in asdex upgrade plasmas in the presence of rf-accelerated nbi ions," Nuclear Fusion **63**, 046001 (2023).
[13] K. G. McClements, R. D'Inca, R. O. Dendy, L. Carbajal, S. C. Chapman, J. W. Cook, R. W. Harvey, W. W. Heidbrink, and S. D. Pinches, "Fast particle-driven ion cyclotron emission (ice) in tokamak plasmas and the case for an ice diagnostic in iter," Nuclear Fusion **55**, 043013 (2015).
[14] R. Ochoukov, K. McClements, R. Bilato, V. Bobkov, B. Chapman, S. Chapman, R. Dendy, M. Dreval, H. Faugel, J.-M. Noterdaeme, M. Salewski, and M. Weiland, "Interpretation of core ion cyclotron emission driven by sub-alfvénic beam-injected ions via magnetoacoustic cyclotron instability: Paper," Nuclear Fusion **59**, 086032 (2019).
[15] D. Moseev, R. Ochoukov, V. Bobkov, R. Dendy, H. Faugel, D. Hartmann, J.-P. Kallmeyer, J. Lansky, H. Laqua, S. Marsen, K. McClements, S. Nielsen, A. Reintrog, M. Salewski, B. Schmidt, T. Schulz, and T. Stange, "Development of the ion cyclotron emission diagnostic for the w7-x stellarator," Review of Scientific Instruments **92**, 033546 (2021).
[16] K. G. McClements, R. O. Dendy, and A. Gondhalekar, "Interpretation of measurements of icrf heated minority proton distributions in jet," Nuclear Fusion **37**, 473–480 (1997).
[17] K. G. McClements, A. Brisset, B. Chapman, S. C. Chapman, R. O. Dendy, P. Jacquet, V. G. Kiptily, M. Mantsinen, B. C. G. Reman, and X. e. a. Litaudon, "Observations and modelling of ion cyclotron emission observed in jet plasmas using a sub-harmonic arc detection system during ion cyclotron resonance heating," Nuclear Fusion **58**, 096020 (2018).
[18] S. Cauffman, R. Majeski, K. McClements, and R. Dendy, "Alfvenic behaviour of alpha particle driven ion cyclotron emission in tftr," Nuclear Fusion **35**, 1597–1602 (1995).
[19] S. G. Thatipamula, G. S. Yun, J. Leem, H. K. Park, K. W. Kim, T. Akiyama, and S. G. Lee, "Dynamic spectra of radio frequency bursts associated with edge-localized modes," Plasma Physics and Controlled Fusion **58**, 065003 (2016).
[20] B. Chapman, R. O. Dendy, K. G. McClements, S. C. Chapman, G. S. Yun, S. G. Thatipamula, and M. H. Kim, "Sub-microsecond temporal evolution of edge density during edge localized modes in kstar tokamak plasmas inferred from ion cyclotron emission," Nuclear Fusion **57**, 124004 (2017).
[21] B. Chapman, R. O. Dendy, S. C. Chapman, K. G. McClements, G. S. Yun, S. G. Thatipamula, and M. H. Kim, "Interpretation of suprathermal emission at deuteron cyclotron harmonics from deuterium plasmas heated by neutral beam injection in the kstar tokamak," Nuclear Fusion **59**, 106021 (2019).
[22] B. Chapman, R. O Dendy, S. C Chapman, K. G McClements, and R. Ochoukov, "Origin of ion cyclotron emission at the proton cyclotron frequency from the core of deuterium plasmas in the asdex-upgrade tokamak," Plasma Physics and Controlled Fusion **62**, 095022 (2020).
[23] K. Saito, H. Kasahara, T. Seki, R. Kumazawa, T. Mutoh, T. Watanabe, F. Shimpo, G. Nomura, M. Osakabe, M. Ichimura, H. Higaki, and A. Komori, "Measurement of ion cyclotron emissions by use of icrf heating an-

tennas in lhd," Fusion Engineering and Design **84**, 1676–1679 (2009).
[24]E. A. Veshchev, T. Ozaki, P. R. Goncharov, S. Sudo, and L. E. Group, "Fast particle loss-cone measurements by angular resolved multi-sightline neutral particle analyzer (arms-npa) in large helical device (lhd)," Journal of Plasma and Fusion Research SERIES **8**, 1084–1088 (2009).
[25]A. Bustos, F. Castejón, M. Osakabe, L. A. Fernández, V. Martin-Mayor, J. Guasp, and J. M. Fontdecaba, "Kinetic simulations of fast ions in stellarators," Nuclear Fusion **51**, 083040 (2011).
[26]T. Ozaki, E. Veshchev, T. Ido, A. Shimizu, P. Goncharov, and S. Sudo, "Perpendicular and tangential angularly resolved multi-sight neutral particle analyzer system in lhd," Review of Scientific Instruments **83**, 10D920 (2012).
[27]B. C. G. Reman, "Doctoral dissertation," (2018).
[28]B. C. Reman, R. O. Dendy, T. Akiyama, S. C. Chapman, J. W. Cook, H. Igami, S. Inagaki, K. Saito, and G. S. Yun, "Interpreting observations of ion cyclotron emission from large helical device plasmas with beam-injected ion populations," Nuclear Fusion **59**, 096013 (2019).
[29]S. Sumida, K. Shinohara, R. Ikezoe, M. Ichimura, M. Sakamoto, M. Hirata, and S. Ide, "Comparison of dispersion model of magneto-acoustic cyclotron instability with experimental observation of3he ion cyclotron emission on jt-60u," Journal of the Physical Society of Japan **86**, 124501 (2017).
[30]S. Sumida, K. Shinohara, R. Ikezoe, M. Ichimura, M. Sakamoto, M. Hirata, and S. Ide, "Study on ion cyclotron emission excited by dd fusion produced ions on jt-60u," 45th Eps Conference on Plasma Physics, Eps 2018 **2018-**, 589–592 (2018).
[31]S. Sumida, K. Shinohara, M. Ichimura, T. Bando, A. Bierwage, and S. Ide, "Identification of slow-wave ion cyclotron emission on jt-60u," Nuclear Fusion **61**, 116036 (2021).
[32]A. I. Zalzali, K. E. Thome, R. O. Dendy, B. Chapman, S. C. Chapman, J. W. Cook, M. A. van Zeeland, N. A. Crocker, and G. H. DeGrandchamp, "Simulations of ion cyclotron emission from diii-d tokamak plasmas," 47th Eps Conference on Plasma Physics, Eps 2021 **2021-**, 784–787 (2021).
[33]K. E. Thome, D. C. Pace, R. I. Pinsker, M. A. Van Zeeland, W. W. Heidbrink, and M. E. Austin, "Central ion cyclotron emission in the diii-d tokamak," Nuclear Fusion **59**, 086011 (2019).
[34]G. H. DeGrandchamp, J. B. Lestz, M. A. Van Zeeland, X. D. Du, W. W. Heidbrink, K. E. Thome, N. A. Crocker, and R. I. Pinsker, "Mode structure measurements of ion cyclotron emission and sub-cyclotron modes on diii-d," Nuclear Fusion **62**, 106033 (2022).
[35]L. Liu, X. Zhang, Y. Zhu, C. Qin, Y. Zhao, S. Yuan, Y. Mao, M. Li, K. Zhang, J. Cheng, L. Ai, and Y. Cheng, "Ion cyclotron emission driven by deuterium neutral beam injection and core fusion reaction ions in east," Nuclear Fusion **60**, 044002 (2020).
[36]L. Liu, R. Ochoukov, K. McClements, R. Dendy, V. Bobkov, M. Weiland, R. Bilato, H. Faugel, D. Moseev, M. Salewski, W. Zhang, X. Zhang, Y. Zhu, B. Chapman, and A. Zalzali, "Explanation of core ion cyclotron emission from beam-ion heated plasmas in asdex upgrade by the magnetoacoustic cyclotron instability," Nuclear Fusion **61**, 026004 (2021).
[37]M. Salewski, B. Geiger, A. S. Jacobsen, M. García-Muñoz, W. Heidbrink, S. B. Korsholm, F. Leipold, J. Madsen, D. Moseev, S. K. Nielsen, J. Rasmussen, M. Stejner Pedersen, G. Tardini, and M. Weiland, "Measurement of a 2d fast-ion velocity distribution function by tomographic inversion of fast-ion d-alpha spectra," Nuclear Fusion **54**, 023005 (2014).
[38]M. Weiland, B. Geiger, A. S. Jacobsen, M. Reich, M. Salewski, and T. Odstrčil, "Enhancement of the fida diagnostic at asdex upgrade for velocity space tomography," Plasma Physics and Controlled Fusion **58**, 025012 (2016).
[39]M. Salewski, B. Geiger, A. Jacobsen, P. C. Hansen, W. Heidbrink, S. B. Korsholm, F. Leipold, J. Madsen, D. Moseev, S. K. Nielsen, M. Nocente, T. Odstrčil, J. Rasmussen, L. Stagner, M. S. Pedersen, and M. Weiland, "High-definition velocity-space tomography of fast-ion dynamics," Nuclear Fusion **56**, 106024 (2016).
[40]M. Weiland, R. Bilato, B. Geiger, P. A. Schneider, G. Tardini, M. Garcia-Munoz, F. Ryter, M. Salewski, and H. Zohm, "Phase-space resolved measurement of 2nd harmonic ion cyclotron heating using fida tomography at the asdex upgrade tokamak: Paper," Nuclear Fusion **57**, 116058 (2017).
[41]B. Madsen, M. Salewski, J. Huang, A. Jacobsen, O. Jones, and K. G. McClements, "Velocity-space tomography using prior information at mast," Review of Scientific Instruments **89**, 10D125 (2018).
[42]B. Madsen, M. Salewski, W. Heidbrink, L. Stagner, M. Podestà, D. Lin, A. Garcia, P. C. Hansen, and J. Huang, "Tomography of the positive-pitch fast-ion velocity distribution in diii-d plasmas with alfvén eigenmodes and neoclassical tearing modes," Nuclear Fusion **60**, 066024 (2020).
[43]B. Madsen, J. Huang, M. Salewski, H. Järleblad, P. Hansen, L. Stagner, J. Su, J. F. Chang, J. Fu, J. F. Wang, L. Z. Liang, G. Q. Zhong, Y. Y. Li, B. Lyu, H. Q. Liu, Q. Zang, Z. P. Luo, M. Nocente, D. Moseev, T. S. Fan, Y. M. Zhang, D. Yang, J. Q. Sun, and L. Y. Liao, "Fast-ion velocity-space tomography using slowing-down regularization in east plasmas with co- and counter-current neutral beam injection: Paper," Plasma Physics and Controlled Fusion **62**, 115019 (2020).
[44]J. Su, B. Wan, J. Huang, B. Madsen, M. Salewski, Y. Sun, J. Wang, J. Fu, J. Chang, C. Wu, L. Liang, Y. Chen, G. Zhong, H. Liu, Q. Zang, Y. Li, B. Lyu, J. Qian, and X. Gong, "Reconstructions of velocity distributions from fast-ion d-alpha (fida) measurements on east," Plasma Science and Technology **23**, 095103 (2021).
[45]A. S. Jacobsen, M. Salewski, B. Geiger, S. B. Korsholm, F. Leipold, S. K. Nielsen, J. Rasmussen, M. S. Pedersen, and M. Weiland, "Benchmark and combined velocity-space tomography of fast-ion d-alpha spectroscopy and collective thomson scattering measurements," Plasma Physics and Controlled Fusion **58**, 042002 (2016).
[46]M. Salewski, M. Nocente, A. S. Jacobsen, F. Binda, C. Cazzaniga, G. Ericsson, J. Eriksson, G. Gorini, C. Hellesen, A. Hjalmarsson, V. Kiptily, T. Koskela, S. B. Korsholm, T. Kurki-Suonio, F. Leipold, J. Madsen, D. Moseev, S. K. Nielsen, J. Rasmussen, M. Schneider, S. Sharapov, M. S. Pedersen, and M. Tardocchi, "Mev-range velocity-space tomography from gamma-ray and neutron emission spectrometry measurements at jet," Nuclear Fusion **57**, 056001 (2017).
[47]M. Salewski, M. Nocente, A. Jacobsen, F. Binda, C. Cazzaniga, J. Eriksson, B. Geiger, G. Gorini, C. Hellesen, V. G. Kiptily, T. Koskela, S. Korsholm, T. Kurki-Suonio, F. Leipold, D. Moseev, S. K. Nielsen, J. Rasmussen, P. A. Schneider, S. E. Sharapov, M. Stejner, and M. Tardocchi, "Bayesian integrated data analysis of fast-ion measurements by velocity-space tomography," Fusion Science and Technology **74**, 23–36 (2018).
[48]J. Galdon-Quiroga, M. Garcia-Munoz, K. G. McClements, M. Nocente, M. Hoelzl, A. Jacobsen, F. Orain, J. F. Rivero-Rodriguez, M. Salewski, L. Sanchis-Sanchez, W. Suttrop, and E. Viezzer, "Beam-ion acceleration during edge localized modes in the asdex upgrade tokamak," Physical Review Letters **121**, 025002 (2018).
[49]J. Galdon-Quiroga, M. Garcia-Munoz, K. G. McClements, M. Nocente, S. S. Denk, S. Freethy, A. S. Jacobsen, F. Orain, J. F. Rivero-Rodriguez, M. Salewski, L. Sanchis-Sanchez, W. Suttrop, E. Viezzer, and M. Willensdorfer, "Observation of accelerated beam ion population during edge localized modes in the asdex upgrade tokamak," Nuclear Fusion **59**, 066016 (2019).
[50]M. Salewski, M. Nocente, B. Madsen, I. Abramovic, G. Gorini, A. S. Jacobsen, V. Kiptily, S. B. Korsholm, D. Moseev, S. K. Nielsen, A. F. L. Poulsen, J. Rasmussen, M. Tardocchi, B. Geiger, and J. Eriksson, "Diagnostic of fast-ion energy spectra and densities in magnetized plasmas," Journal of Instrumentation **14**, C05019 (2019).
[51]B. S. Schmidt, M. Salewski, B. Reman, R. O. Dendy, D. Moseev, R. Ochoukov, A. Fasoli, M. Baquero-Ruiz, and H. Järleblad, "Determining 1d fast-ion velocity distribution functions from ion cyclotron emission data using deep neural networks," Review of Scientific Instruments **92**, 053528 (2021).
[52]L. Stagner, W. W. Heidbrink, M. Salewski, A. S. Jacobsen, and B. Geiger, "Orbit tomography of energetic particle distribution functions," Nuclear Fusion **62**, 026033 (2022).
[53]M. Salewski, B. Geiger, D. Moseev, W. W. Heidbrink, A. S. Jacobsen, S. B. Korsholm, F. Leipold, J. Madsen, S. K. Nielsen, J. Rasmussen, M. Stejner Pedersen, and M. Weiland, "On velocity-space sensitivity of fast-ion d-alpha spectroscopy," Plasma Physics and Controlled Fusion **56**, 105005 (2014).
[54]W. W. Heidbrink, Y. Luo, K. H. Burrell, R. W. Harvey, R. I. Pinsker, and E. Ruskov, "Measurements of fast-ion acceleration at cyclotron harmonics using balmer-alpha spectroscopy," Plasma Physics and Controlled Fusion **49**, 1457–1475 (2007).
[55]M. Salewski, S. K. Nielsen, H. Bindslev, V. Furtula, N. Gorelenkov, S. B. Korsholm, F. Leipold, F. Meo, P. Michelsen, D. Moseev, and M. Stejner Pedersen, "On velocity space interrogation regions of fast-ion collective thomson scattering at iter," Nuclear Fusion **51**, 083014 (2011).

[56]J. Galdon-Quiroga, M. Garcia-Munoz, M. Salewski, A. Jacobsen, L. Sanchis-Sanchez, M. Rodriguez-Ramos, J. Ayllon-Guerola, J. Garcia-Lopez, J. Gonzalez-Martin, M. Jimenez-Ramos, J. Rivero-Rodriguez, and E. Viezzer, "Velocity-space sensitivity and tomography of scintillator-based fast-ion loss detectors," Plasma Physics and Controlled Fusion **60**, 105005 (2018).

[57]M. Salewski, M. Nocente, G. Gorini, A. S. Jacobsen, V. Kiptily, S. B. Korsholm, F. Leipold, J. Madsen, D. Moseev, S. K. Nielsen, J. Rasmussen, M. S. Pedersen, and M. Tardocchi, "Velocity-space observation regions of high-resolution two-step reaction gamma-ray spectroscopy," Nuclear Fusion **55**, 093029 (2015).

[58]M. Salewski, M. Nocente, G. Gorini, A. S. Jacobsen, V. Kiptily, S. B. Korsholm, F. Leipold, J. Madsen, D. Moseev, S. K. Nielsen, J. Rasmussen, M. S. Pedersen, and M. Tardocchi, "Fast-ion energy resolution by one-step reaction gamma-ray spectrometry," Nuclear Fusion **56**, 046009 (2016).

[59]A. Jacobsen, F. Binda, C. Cazzaniga, J. Eriksson, A. Hjalmarsson, M. Nocente, M. Salewski, and G. Tardini, "Velocity-space sensitivities of neutron emission spectrometers at the tokamaks jet and asdex upgrade in deuterium plasmas," Review of Scientific Instruments **88**, 073506 (2017).

[60]A. S. Jacobsen, M. Salewski, J. Eriksson, G. Ericsson, S. B. Korsholm, F. Leipold, S. K. Nielsen, J. Rasmussen, and M. Stejner Pedersen, "Velocity-space sensitivity of neutron spectrometry measurements," Nuclear Fusion **55**, 053013 (2015).

[61]J. Eriksson, C. Hellesen, F. Binda, M. Cecconello, S. Conroy, G. Ericsson, L. Giacomelli, G. Gorini, A. Hjalmarsson, V. G. Kiptily, M. Mantsinen, M. Nocente, A. Sahlberg, M. Salewski, S. Sharapov, and M. Tardocchi, "Measuring fast ions in fusion plasmas with neutron diagnostics at jet," Plasma Physics and Controlled Fusion **61**, 014027 (2019).

[62]H. Järleblad, L. Stagner, M. Salewski, J. Eriksson, S. Benjamin, B. Madsen, M. Nocente, J. Rasmussen, and B. Schmidt, "Fast-ion orbit sensitivity of neutron emission spectroscopy diagnostics," Review of Scientific Instruments **92**, 043526 (2021).

[63]H. Järleblad, L. Stagner, M. Salewski, J. Eriksson, M. Nocente, J. Rasmussen, Štancar, Y. O. Kazakov, and B. Simmendefeldt, "Fast-ion orbit sensitivity of neutron and gamma-ray diagnostics for one-step fusion reactions," Nuclear Fusion **62**, 112005 (2022).

[64]W. Heidbrink, A. Garcia, W. Boeglin, and M. Salewski, "Phase-space sensitivity (weight functions) of 3 mev proton diagnostics," Plasma Physics and Controlled Fusion **63**, 055008 (2021).

[65]C. G. Darwin, "Li. the dynamical motions of charged particles," The london, edinburgh, and dublin philosophical magazine and journal of science **39**, 537–551 (1920).

[66]B. C. Reman, R. O. Dendy, T. Akiyama, S. C. Chapman, J. W. Cook, H. Igami, S. Inagaki, K. Saito, R. Seki, M. H. Kim, S. G. Thatipamula, and G. S. Yun, "Density dependence of ion cyclotron emission from deuterium plasmas in the large helical device," Nuclear Fusion **61**, 066023 (2021).

[67]B. C. Reman, R. O. Dendy, H. Igami, T. Akiyama, M. Salewski, S. C. Chapman, J. W. Cook, S. Inagaki, K. Saito, R. Seki, M. Toida, M. H. Kim, S. G. Thatipamula, and G. S. Yun, "First observation and interpretation of spontaneous collective radiation from fusion-born ions in a stellarator plasma," Plasma Physics and Controlled Fusion **64**, 085008 (2022).

[68]L. Carbajal-Gomez, *Transport in turbulent plasmas at the interface between different levels of description*, Ph.D. thesis, University of Warwick (2015).

[69]L. Carbajal, R. O. Dendy, S. C. Chapman, and J. W. S. Cook, "Linear and nonlinear physics of the magnetoacoustic cyclotron instability of fusion-born ions in relation to ion cyclotron emission," Physics of Plasmas **21**, 012106 (2014).

[70]D. Moseev and M. Salewski, "Bi-maxwellian, slowing-down, and ring velocity distributions of fast ions in magnetized plasmas," Physics of Plasmas **26**, 020901 (2019).

[71]S. Cauffman and R. Majeski, "Ion-cyclotron emission on the tokamak fusion test reactor," Review of Scientific Instruments **66**, 817–819 (1995).

[72]M. Ichimura, H. Higaki, S. Kakimoto, Y. Yamaguchi, K. Nemoto, M. Katano, M. Ishikawa, S. Moriyama, and T. Suzuki, "Observation of spontaneously excited waves in the ion cyclotron frequency range on jt-60u," Nuclear Fusion **48**, 035012 (2008).

[73]S. Sato, M. Ichimura, Y. Yamaguchi, M. Katano, Y. Imai, T. Murakami, Y. Miyake, T. Yokoyama, S. Moriyama, T. Kobayashi, A. Kojima, K. Shinohara, Y. Sakamoto, T. Watanabe, H. Hojo, and T. Imai, "Observation of ion cyclotron emission owing to dd fusion product h ions in jt-60u," Plasma and Fusion Research **5**, S2067 (4 pp.) (2010).

[74]L. N. Liu, X. J. Zhang, Y. B. Zhu, C. M. Qin, Y. P. Zhao, S. Yuan, Y. Z. Mao, M. H. Li, Y. Chen, J. Cheng, L. L. Ping, H. Li, and L. Ai, "Ion cyclotron emission diagnostic system on the experimental advanced superconducting tokamak and first detection of energetic-particle-driven radiation," Review of Scientific Instruments **90**, 063504 (2019).

[75]J. W. Cook, R. O. Dendy, and S. C. Chapman, "Particle-in-cell simulations of the magnetoacoustic cyclotron instability of fusion-born alpha-particles in tokamak plasmas," Plasma Physics and Controlled Fusion **55**, 065003 (2013).

[76]L. Carbajal, R. O. Dendy, S. C. Chapman, and J. W. Cook, "Linear and nonlinear physics of the magnetoacoustic cyclotron instability of fusion-born ions in relation to ion cyclotron emission," Physics of Plasmas **21**, 012106 (2014).

[77]V. S. Belikov and Y. I. Kolesnichenko, "Magnetoacoustic cyclotron instability in a thermonuclear plasma," Sov Phys Tech Phys **20**, 1146–1151 (1975).

[78]B. Chapman, R. O. Dendy, S. C. Chapman, K. G. McClements, G. S. Yun, S. G. Thatipamula, and M. H. Kim, "Nonlinear wave interactions generate high-harmonic cyclotron emission from fusion-born protons during a kstar elm crash," Nuclear Fusion **58**, 096027 (2018).

[79]O. Samant, R. O. Dendy, S. C. Chapman, D. Moseev, and R. Ochoukov, "Predicting the physics of ion cyclotron emission from neutral beam-heated plasmas in the wendelstein 7-x stellarator," 48th EPS Conference on Plasma Physics, EPS 2022 (2022).

[80]K. G. McClements, R. O. Dendy, C. N. Lashmore-Davies, G. A. Cottrell, S. Cauffman, and R. Majeski, "Interpretation of ion cyclotron emission from sub-alfvénic fusion products in the tokamak fusion test reactor," Physics of Plasmas **3**, 543–553 (1996).

[81]R. O. Dendy, B. Chapman-Oplopoiou, B. C. Reman, and J. W. Cook, "Mechanism for collective energy transfer from neutral beam-injected ions to fusion-born alpha particles on cyclotron timescales in a plasma," Physical Review Letters **130**, 105102 (2023).

[82]J. Wesson and D. J. Campbell, "Tokamaks," (2011).

[83]L. Carbajal, R. O. Dendy, S. C. Chapman, and J. W. Cook, "Quantifying fusion born ion populations in magnetically confined plasmas using ion cyclotron emission," Physical Review Letters **118**, 105001 (2017).

[84]R. Dendy, K. McClements, C. LashmoreDavies, G. Cottrell, R. Majeski, and S. Cauffman, "Ion cyclotron emission due to collective instability of fusion products and beam ions in tftr and jet," Nuclear Fusion **35**, 1733–1742 (1995).

[85]P. C. Hansen, *Discrete Inverse Problems: Insight and Algorithms* (Society for Industrial and Applied Mathematics, 2010) pp. xii, 213 Seiten (unknown).

[86]R. Tibshirani, "Regression shrinkage and selection via the lasso," Journal of the Royal Statistical Society Series B-methodological **58**, 267–288 (1996).

[87]M. Salewski, M. Nocente, B. Madsen, I. Abramovic, M. Fitzgerald, G. Gorini, P. Hansen, W. Heidbrink, A. Jacobsen, T. Jensen, V. Kiptily, E. Klinkby, S. Korsholm, T. Kurki-Suonio, A. Larsen, F. Leipold, D. Moseev, S. Nielsen, S. Pinches, J. Rasmussen, M. Rebai, M. Schneider, A. Shevelev, S. Sipilä, M. Stejner, and M. Tardocchi, "Alpha-particle velocity-space diagnostic in iter," Nuclear Fusion **58**, 096019 (2018).

[88]C. K. Birdsall and A. B. Langdon, *Plasma physics via computer simulation* (CRC press, 2004).

[89]R. W. Hockney and J. W. Eastwood, *Computer simulation using particles* (crc Press, 2021).

[90]R. Lee, S. Chapman, and R. Dendy, "Numerical simulations of local shock reformation and ion acceleration in supernova remnants," The Astrophysical Journal **604**, 187 (2004).

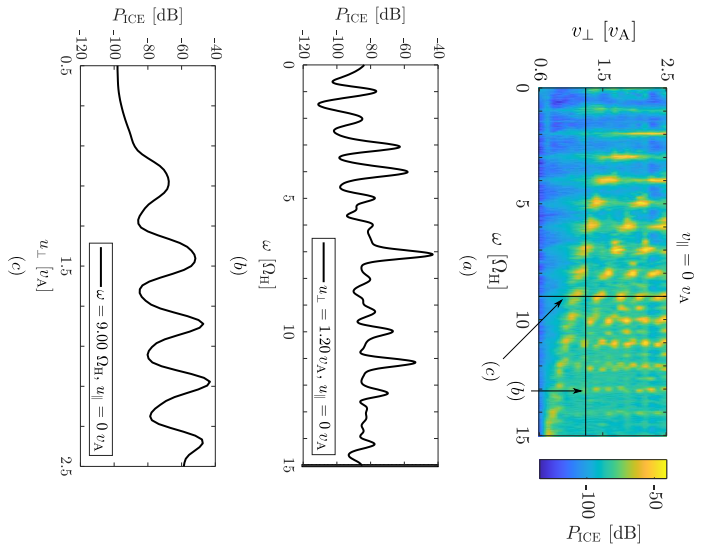

PLEASE CITE THIS ARTICLE AS DOI: 10.1063/5.0157126

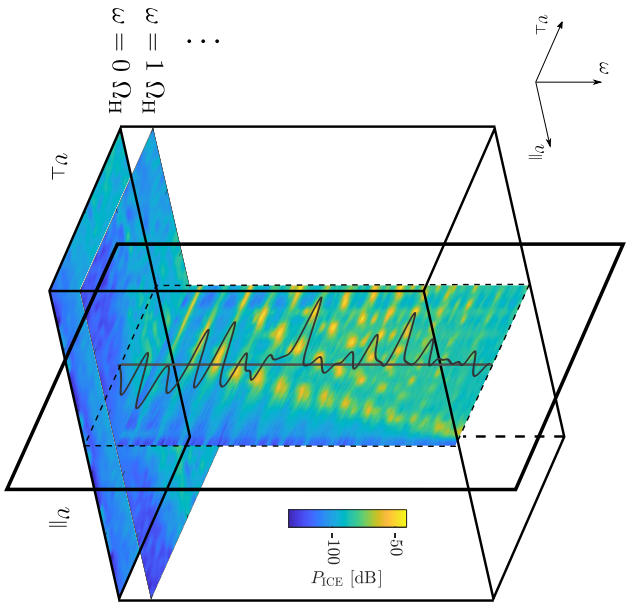

Physics of Plasmas

PLEASE CITE THIS ARTICLE AS DOI: 10.1063/5.0157126

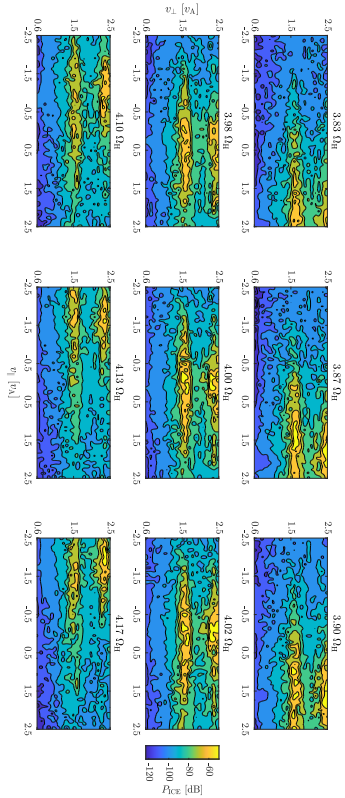

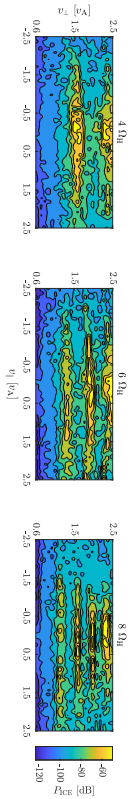

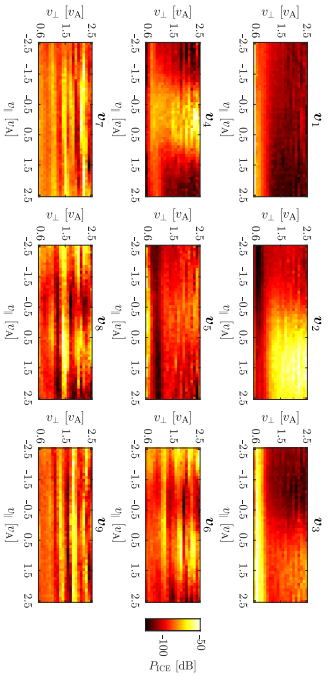

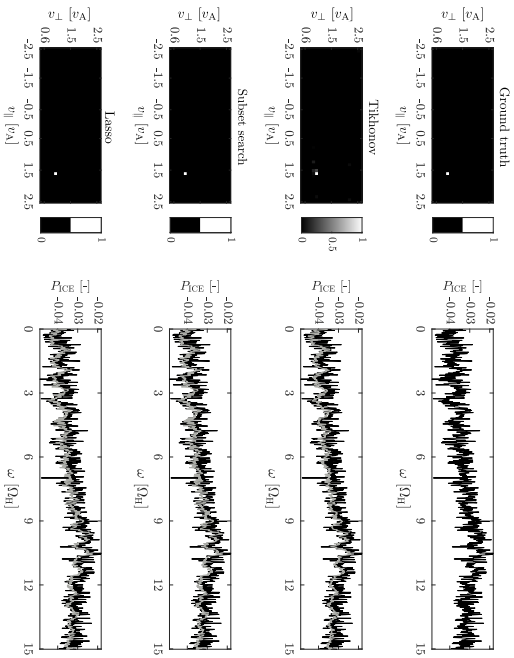

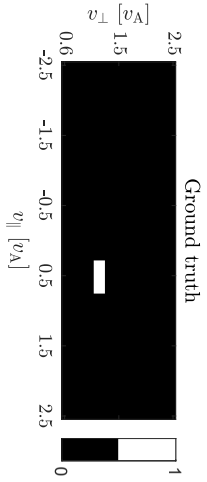

Physics of Plasmas

PLEASE CITE THIS ARTICLE AS DOI: 10.1063/5.0157126